High-Latitude Surface Temperature Estimates from Thermal Satellite Data

Jeffrey R. Key, John B. Collins,* Charles Fowler,[†] and Robert S. Stone[‡]*

T*he surface temperature of the polar regions controls sea ice growth, snow melt, and surface–atmosphere energy exchange. However, our limited knowledge of polar surfaces and atmospheres has hampered the development of methods to estimate surface temperature with satellite data. In this article, clear-sky surface-temperature retrieval algorithms for use with the Advanced Very High Resolution Radiometer (AVHRR) and the Along Track Scanning Radiometer (ATSR) for the Arctic and the Antarctic, over ocean and land, are presented. The methods are similar to those used in estimating sea and land surface temperatures but are developed with data specific to the polar regions. An extensive validation analysis using an annual cycle of surface measurements gives accuracies in the range of 0.3–2.1 K, the larger errors being attributable to the spatially variable surface of the validation area. For homogeneous surfaces the expected accuracy is sufficient for many climate process studies.* ©Elsevier Science Inc., 1997

INTRODUCTION

The annual variation of surface temperature over high-latitude oceans and land can exceed 60°C, and the spatial variation over the polar oceans during winter can approach this value as a result of ice fractures exposing the unfrozen ocean. At all times of the year the surface temperature has a profound influence on sea ice growth, snow metamorphosis, and ice/snow melt. Yet little effort has been directed toward large-scale monitoring of this

*Department of Geography, Boston University
† CCAR, University of Colorado, Boulder
‡ Cooperative Institute for Research in Environmental Sciences, University of Colorado, Boulder

Address correspondence to J. R. Key, Boston Univ., Dept. of Geography, 675 Commonwealth Ave., Boston, MA 02215.

geophysical parameter with satellite data because of our limited knowledge of atmospheric temperature, humidity, and aerosols, cloud microphysical properties, and the spectral characteristics of the wide variety of surface types found at high latitudes. The fact that the first effects of a changing climate are expected to be seen in the high latitudes is persuasion enough that work must be done along these lines.

Key and Haefliger (1992; hereafter KH92) presented an ice surface temperature (IST) retrieval algorithm that was applicable to the central ice pack in the Arctic using data from the Advanced Very High Resolution Radiometer (AVHRR) on NOAA polar-orbiting satellites. Lindsay and Rothrock (1994) performed a comprehensive analysis of the spatial and temporal variability of surface temperature over the entire Arctic basin using the KH92 algorithm. Other investigators have recently presented new methods of estimating high-latitude surface temperature from the AVHRR and the Along Track Scanning Radiometer (ATSR) on ERS-1. For example, Haefliger et al. (1993) used the AVHRR to retrieve surface temperature over Greenland during spring and summer; Stroeve et al. (1996) presented an ATSR algorithm also for use over Greenland during spring and summer; Bamber and Harris (1994) developed a procedure for use with ATSR data based on six stations in Antarctica.

This article also presents procedures for estimating the clear sky surface (skin) temperature at high latitudes using thermal satellite data. The work is a refinement and extension of the procedures in KH92, and is broader in scope than the aforementioned studies. Here we detail algorithms for both the AVHRR and the ATSR, for the Arctic and the Antarctic, over ocean and land.

METHODOLOGY

One approach to estimating surface temperature is to relate satellite observations to surface temperature mea-

surements with a simple regression model. However, for a robust solution a relatively large observational data set is required. Another approach is to model satellite sensor brightness temperatures with a radiative transfer model, and then to relate the modeled brightness temperatures to the surface temperatures used to drive the model. This approach is used here and is commonly used for sea surface temperature (SST) retrieval (e.g., Minnett, 1990; Llewellyn-Jones et al., 1984; Barton, 1985). A more complete review of SST algorithms is given by McClain et al. (1985). For SST estimated using two "split-window" infrared channels at approximately 11 μm and 12 μm an absolute accuracy of 0.5–1 K (root-mean-square error or RMSE) has been obtained (Llewellyn-Jones et al., 1984; McClain et al., 1985). Land surface temperature (LST) estimation is generally less accurate due to the larger variability of surface conditions, where errors of 2–3 K are common (Price, 1983).

In this study surface temperature retrieval algorithms are developed for the AVHRRs on board the NOAA 7, 9, 11, and 12 satellites, and for the ATSR on board ERS-1. Of the five AVHRR channels two thermal channels (Channels 4 and 5 centered at approximately 11 μm and 12 μm, respectively) are used. NOAAs 8 and 10 are not used because they lack a 12 μm channel. The AVHRR scan angle ranges from 0° to approximately 55°. Of the four ATSR channels two thermal channels, centered at approximately 11 μm and 12 μm, are employed. The ATSR instrument is unique in that the sensor views the same ground location from two angles, a forward angle of 55° and a nadir angle. While the sensor does also scan across track from 0° to approximately 22°, only the forward and nadir angle views are used in the surface temperature retrieval.

For the retrieval of SST, a multichannel algorithm that corrects for atmospheric attenuation of upwelling radiation primarily due to water vapor absorption is commonly employed (e.g., Barton et al., 1989):

$$T_s = a(\theta) + \sum_{i=1}^{n} b_i(\theta) T_i, \qquad (1)$$

where θ is the satellite scan angle, $a(\theta)$ and $b_i(\theta)$ are scan angle-dependent coefficients and T_i are the measured brightness temperatures in each thermal channel i of n. For the ATSR, the scan angle is an implicit part of (1). The coefficients are determined through a least squares regression procedure, where surface temperatures are regressed against modeled brightness temperatures. Brightness temperature differences and/or ratios between two channels may also be used (e.g., Schluessel and Grassl, 1990).

To simulate radiances in the AVHRR and ATSR thermal channels, daily temperature and humidity profiles are used with a radiative transfer model. Radiosonde ascents over the northern hemisphere are taken from three archives: the North Pole archive, the NCAR ar-
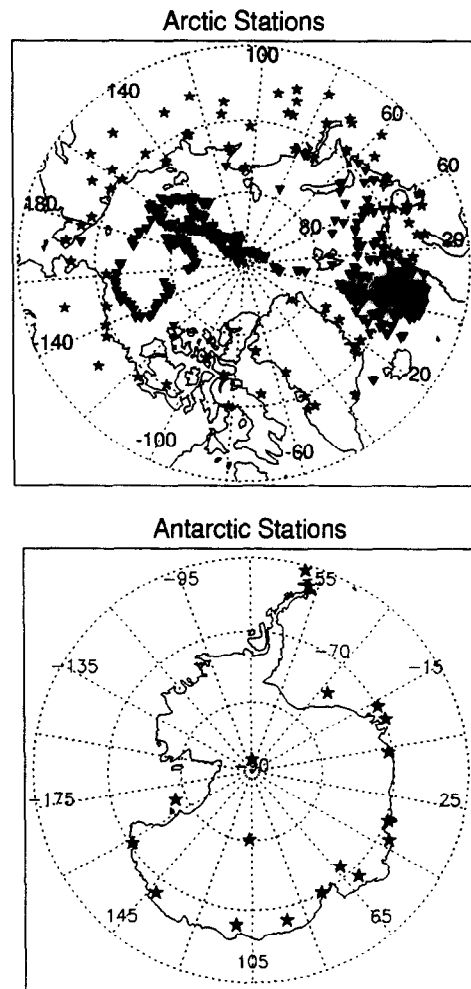
Arctic Stations

Antarctic Stations

Figure 1. Arctic (top) and Antarctic (bottom) locations that comprise the radiosonde profile data set used in the modeling of satellite radiances. For the Arctic, stars indicate those stations used in the land algorithm; triangles show the stations used in the ocean algorithm.

chive, and the Historical Arctic Rawinsonde archive (Serreze et al., 1992). Soundings are sampled from these three archives over the entire Arctic, over land, ocean, and sea ice north of 65°N latitude for the period 1978–1991. For the Arctic ice surface temperature algorithm more than 1000 drifting ice and coastal station radiosonde profiles were used. The Arctic snow-free land algorithms are based on approximately 800 profiles from 37 coastal and interior stations. Profile data for Antarctica are taken from the Antarctic Radiosonde Data Set (Connolley and King, 1993), a compilation of data from 18 land stations, including 16 coastal stations and two interior stations over the period 1982–1990. More than 1000 profiles were used in the Antarctic analysis. Surface temperature algorithms for the Antarctic do not distinguish between land and frozen ocean because only a very
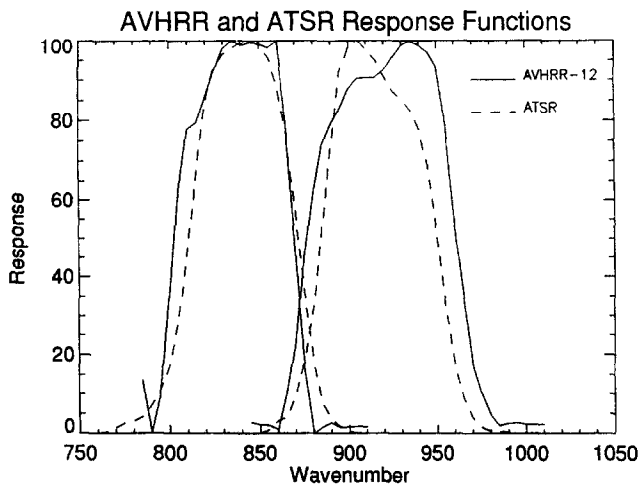
AVHRR and ATSR Response Functions

Figure 2. Comparison of the ATSR (ERS-1) and the AVHRR (NOAA 12) response functions (%) for the 11 μm and 12 μm thermal channels.

Table 1. Modeled Angular Emissivities of Snow in NOAA 7 AVHRR Channels 4 and 5

Scan Angle (degrees)	Channel 4 Emissivity	Channel 5 Emissivity
0	0.9988	0.9961
10	0.9987	0.9958
20	0.9984	0.9949
30	0.9977	0.9933
40	0.9968	0.9908
50	0.9955	0.9872

small percentage of the land area is ever snow-free. Figure 1 shows the locations of the radiosonde stations.

The radiative transfer model used to simulate the satellite sensor radiances is LOWTRAN 7 (hereafter LOWTRAN) (Kneizys et al., 1988). Earlier versions of LOWTRAN have been used in the retrieval of SST (Barton et al., 1989; KH92). LOWTRAN calculates atmospheric transmittance/radiance for wave numbers ranging from 0 to 50,000 cm^{-1} (wavelengths of 0.2 μm to infinity) and includes calculations for multiple scattering. Radiances are calculated at 5 cm^{-1} intervals, interpolated by LOWTRAN from 20 cm^{-1} absorption intervals. The AVHRR calculations are done for sensor scan angles from 0° to 60° in 10° increments. For the ATSR, nadir and forward radiances are modeled at 0° and 55°, respectively. LOWTRAN's built-in subarctic winter and summer profiles of trace gases and aerosols are used. Blanchet and List (1983) show that the volume extinction coefficient of Arctic haze is generally of the same order of magnitude as that of tropospheric aerosols, so that tropospheric background aerosols amounts are used. Sensor response functions for NOAA 7, 9, 11, 12 and ERS-1 ATSR (Fig. 2) are applied to the calculated radiances, and then radiances are converted to brightness temperatures by inverting the Planck function at the channel central wavelength appropriate for the temperature range 230–270 K (NOAA, 1991).

ICE SURFACE TEMPERATURE

For ice/snow surface temperature (IST) retrieval from the AVHRR we use the equation

$$T_s = a + bT_{11} + c(T_{11} - T_{12}) + d[(T_{11} - T_{12})(\sec \theta - 1)], \quad (2)$$

where T_s is the estimated surface temperature (K), T_{11} and T_{12} are the brightness temperatures (K) at 11 μm (AVHRR Channel 4) and 12 μm (Channel 5), and θ is the sensor scan angle. KH92 used a very similar form,

though this form was found to be superior. Coefficients a, b, c, and d are derived for the following temperature ranges: $T_{11} < 240$ K, 240 K $< T_{11} < 260$ K, $T_{11} > 260$ K. The use of temperature ranges rather than the seasons defined in KH92 provides greater flexibility in the algorithm. For example, the central Arctic during winter is typically much warmer than the Atlantic side of the Arctic. Using seasons defined by calendar months would result in the same set of coefficients being used in both locations.

For the ATSR we use the relationship

$$T_s = a + bT_{11, nadir} + cT_{11, forward} + dT_{11, nadir} + eT_{12, forward}, \quad (3)$$

where T_{11} and T_{12} are the brightness temperatures of the 11 μm and 12 μm channels in Kelvin and the subscripts nadir and forward refer to the two viewing angles.

For ice/snow surface temperature retrieval, the surface is assumed to be snow-covered. Directional emissivities for snow are modelled following the procedure of Dozier and Warren (1982). Briefly, the single scattering albedo and asymmetry factor are calculated from the Mie equations, and the directional, wavelength-dependent emissivities are derived from the Delta-Eddington approximation to the radiative transfer equation. The directional emissivities are then integrated with the response function for channel i:

$$\varepsilon_i(\theta) = \frac{\int_{\lambda_1}^{\lambda_2} \varepsilon(\lambda, \theta)\varphi_i(\lambda)\, d\lambda}{\int_{\lambda_1}^{\lambda_2} \varphi_i(\lambda)\, d\lambda}, \quad (4)$$

where $\varepsilon(\lambda, \theta)$ is the emissivity in direction θ at wavelength λ and φ_i is the sensor response function which is 0 outside of $[\lambda_1, \lambda_2]$. The channel-integrated emissivities for snow are given in Table 1. At the wavelengths used here Dozier and Warren (1982) found that the emissivity is essentially insensitive to snow grain size as well as the amount of liquid water, up to 20% of the total particle volume. Additionally, these emissivities do not change significantly over the range of temperatures encountered. However, recent laboratory measurements (Salisbury et al., 1994) have shown that snow grain size and packing fraction are important, although for naturally occurring snow the angular effects may still dominate (Wald, 1994). As in KH92 and Stroeve et al. (1996), we employ the modeling method described above, noting that the ef-

Table 2. AVHRR Arctic Snow/Ice Coefficients for Use with Equation 2

Satellite	Temperature Range	a	b	c	d
NOAA 7	<240 K	-3.82468	1.01452	2.22875	-1.29408
	240-260 K	-4.60504	1.01761	1.79531	-0.08029
	>260 K	-4.41581	1.01648	1.66647	0.68402
NOAA 9	<240 K	-5.48207	1.02179	1.99583	-1.18365
	240-260 K	-6.54114	1.02586	1.64728	0.27868
	>260 K	-5.25491	1.02043	1.63575	1.14777
NOAA 11	<240 K	-4.65532	1.01810	2.19679	-1.26894
	240-260 K	-5.39334	1.02096	1.76399	0.04116
	>260 K	-4.76934	1.01813	1.66489	0.84750
NOAA 12	<240 K	-2.79827	1.01039	2.10004	-1.02716
	240-260 K	-3.47596	1.01312	1.68157	-0.01882
	>260 K	-4.12109	1.01502	1.66900	0.54726

Table 3. AVHRR Antarctic Snow/Ice Coefficients for Use with Equation 2

Satellite	Temperature Range	a	b	c	d
NOAA 7	<240 K	-1.21619	1.00433	1.36556	-0.65060
	240-260 K	-6.40072	1.02561	0.98103	0.56256
	>260 K	-7.00035	1.02736	1.07976	0.88936
NOAA 9	<240 K	-1.76282	1.00745	0.47768	-0.08011
	240-260 K	-8.08351	1.032878	0.60057	1.15843
	>260 K	-7.98541	1.03176	0.92139	1.43351
NOAA 11	<240 K	-1.46611	1.00567	1.09288	-0.47756
	240-260 K	-7.10043	1.02863	0.85709	0.76661
	>260 K	-7.39846	1.02914	1.03573	1.07391
NOAA 12	<240 K	-0.80019	1.00228	1.72955	-0.75776
	240-260 K	-4.82371	1.01908	1.13866	0.38312
	>260 K	-6.11450	1.02361	1.17492	0.67614

fects of wind, snow age, and topography, of which we know nothing *a priori*, may also be important. For temperatures above the melting point, a mixture of snow/ice and meltponds is assumed. The emissivity is a weighted sum of snow and fresh-water emissivities, where the weights are 0.8 for snow and 0.2 for water. This is only an approximation, however, as the area fraction of snow and melt ponds can be very different from these values.

The procedure to determine (2) and (3) is summarized as follows. Modeled emissivities and observed temperature and humidity profiles are used with LOWTRAN to estimate radiances at the satellite. In the radiative transfer calculations the temperature of the first level, essentially a shelter temperature, is used as the surface (skin) temperature. (In KH92 the skin temperature was modeled using an energy balance approach. Any gain in accuracy attributable to that approach would be lost here as a result of the greater variety of surface types and geographical regions considered; that is, it would be difficult to define an appropriate set of boundary layer conditions applicable to all surface types and locations.) The modeled radiances are integrated with the sensor response functions for the AVHRR and ATSR channels and then converted to brightness temperatures. A least-squares multiple linear regression is used to determine the coefficients in (2) and (3). These are given in Tables 2–4 as a function of the clear-sky 11 μm temperature in three ranges. Correlations between estimated and actual surface temperatures in the regression analysis are greater than 0.97 in all cases. RMS errors range from less than 0.1 to 0.3 K, the larger values corresponding to the higher temperature category. With the two scan angles, the ATSR algorithm produced an RMS error more than 0.1 K smaller than that of the AVHRR at higher temperatures.

SNOW-FREE LAND SURFACE TEMPERATURE

Algorithms designed to retrieve ice or sea surface temperature from remotely sensed thermal radiances cannot be applied to snow-free land surfaces. This is because emissivity over land surfaces tends to be somewhat lower than that of snow, and also exhibits important spectral and temporal variations (Wan and Dozier, 1989). Additionally, land surface temperature itself varies at relatively high spatial frequencies, so that the best one can hope to estimate is an "area-average" surface temperature within the sensor field of view.

For snow-free land surface temperature retrieval, radiative transfer theory can be used to derive relationships between surface temperature, split-window radiances, and spectral emissivities (e.g., Price, 1984; Becker and Li, 1990; Sobrino et al., 1994). The independent variables in these models are mathematical combinations of ε_{11}, ε_{12}, T_{11}, and T_{12}, the emissivities and brightness temperatures at 11 μm and 12 μm. Prata (1993) shows that the unknown parameters of these models can be related to physical properties of the atmosphere and the land surface, so knowledge of these parameters allows for the determination of surface temperature from satellite data. Although some studies include standard Arctic atmospheres in their radiative transfer simulations (e.g., Becker and Li, 1990), none base their calculations exclusively on observed high-latitude atmospheric profiles. To derive a split-window algorithm specifically for Arctic land areas, the same modeling approach as that used for ice surface temperature was followed.

The modeled relationship between surface emissivity and brightness temperature is very nearly linear in the emissivity range of 0.90–1.00. So it is possible to model brightness temperatures in each spectral band at emissivities of 0.90 and 1.00, and to calculate brightness temperatures at arbitrary emissivities by linear interpolation. Brightness temperatures in the 11 μm band were thus determined for emissivities of 0.90, 0.95, and 1.00. For each value of ε_{11}, the 12 μm brightness temperature was determined using spectral emissivity differences $(\varepsilon_{11} - \varepsilon_{12})$ of -0.01, -0.005, 0.0, 0.005, and 0.01, except where this would result in a value of ε_{12} exceeding 1.0. These values encompass the range of measured emissivities of Arctic land cover types given by Rees (1993), and provide for

Table 4. ASTR Arctic and Antarctic Snow/Ice Coefficients for Use with Equation 3

Polar Region	Temperature Range	a	b	c	d	e
Arctic	<240 K	−0.34213	0.66340	−0.15849	1.38082	−0.88586
	240–260 K	−0.79801	1.50374	−0.45245	0.33780	−0.38684
	>260 K	−0.56158	2.23152	−0.91817	−0.40756	0.09610
Antarctic	<240 K	0.00314	1.060343	−0.42877	1.04872	−0.68183
	240–260 K	−0.95689	1.86848	−0.75113	0.00039	−0.11458
	>260 K	−0.60407	1.89027	−0.58023	−0.14938	−0.15887

realistic emissivity differences between the two split window channels (e.g., Prata, 1994a,b). The regression method of relating modeled brightness temperatures to surface temperature was used for the snow-free land algorithm with the following differences: 1) radiosonde profiles only from land stations were used, and the latitudinal range was extended southward to 65°N (Fig. 1), 2) because spectral emissivities at 11 μm and 12 μm are spatially variable and generally unknown, they are variables in the regression, and 3) scan angle is not a variable in the regression since the dependence of emissivity on view angle is unknown. The regression model for snow-free land using the AVHRR and ATSR is

$$T_s = a + bT_{11} + cT_{12} + d\varepsilon_{11} + e\varepsilon_{12}. \qquad (5)$$

Although (5) is a simple linear combination of emissivities and brightness temperatures, it performs with the same level of accuracy as models that contain more explicit physics. For example, refitting the model given by Price (1984) with the same data simulated in this study results in a root-mean-squared error for our model that is slightly lower than that obtained by Price's model. Following the scheme for ice-covered ocean and snow-covered land, models for snow-free land are developed for the three different temperature ranges. Coefficients are given in Table 5. As with the snow/ice regressions, corre-

lations are high, greater than 0.97 in all cases. RMS errors are also similar (from less than 0.1–0.3 K), though slightly larger (0.4 K) at higher temperatures due to greater variability in atmospheric moisture.

DISCUSSION

What is the magnitude of the atmospheric corrections implicit in (2), (3), and (5)? Given the low water vapor content of polar atmospheres and the near-unit emissivities of snow and ice, one would expect the difference between the actual surface temperature and the 11 μm brightness temperature to be small. Figure 3 illustrates the magnitude of this difference over the temperature range typical of high latitude regions. Results are shown for two scan angles: nadir and 50°. At low temperatures atmospheric attenuation is minimal, and the 11 μm brightness temperature itself is a good estimate of the surface temperature. In contrast, at higher summer temperatures the difference between the brightness temperature and the surface temperature can be 3° or more. Also shown is the influence of the near-unit emissivity in the retrieval of surface temperature. The lines in the figure show the differences between 11 μm brightness temperatures and blackbody temperatures for snow emissivities at nadir and 50° viewing angles. They were deter-

Table 5. AVHRR and ATSR Polar Land Coefficients for Use with Equation 5

| Satellite	Temperature Range	a	b	c	d	e
NOAA 7	<240 K	26.0309	4.0147	−2.9919	−165.0710	133.5685
	240–260 K	32.1194	3.5683	−2.5444	−164.3970	126.3626
	>260 K	44.4224	3.6507	−2.6387	−181.1707	133.4351
NOAA 9	<240 K	23.0055	4.4368	−3.4103	−181.5454	152.2116
	240–260 K	29.3755	3.6499	−2.6167	−167.8258	130.4036
	>260 K	41.5469	3.7915	−2.7710	−188.3021	141.5502
NOAA 11	<240 K	24.5757	4.2369	−3.2127	−173.8222	143.4666
	240–260 K	30.9222	3.5992	−2.5714	−165.6568	127.9483
	>260 K	43.0879	3.7034	−2.6874	−183.7980	136.5114
NOAA 12	<240 K	29.1836	3.4836	−2.4606	−144.4215	109.7186
	240–260 K	34.8680	3.5896	−2.5732	−166.2492	127.2383
	>260 K	46.9049	3.6529	−2.6470	−181.5388	132.7192
ATSR	<240 K	30.0063	3.6227	−2.6021	−151.2939	116.3105
	240–260 K	35.7733	4.1795	−3.1719	−195.1314	157.2663
	>260 K	46.6237	3.6624	−2.6527	−182.4819	132.8915

T_S-T_4 from Lowtran
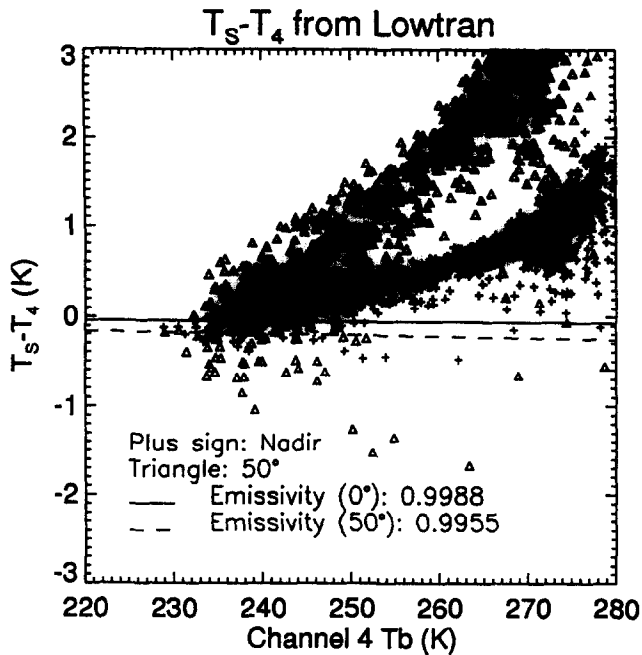
Figure 3. The difference between the surface temperature and the modeled 11 μm brightness temperature (T_4) over a range of temperatures at two scan angles. Also shown is the difference between the blackbody and brightness temperatures for two surface emissivities.

mined by inverting the Planck function and therefore indicate the effect of emissivity alone in the retrieval of snow (and approximately ice) surface temperature. The figure shows that emissivity differences in the temperature range examined here are small relative to the atmospheric effects.

Inclusion of AVHRR Channel 3 (3.7 μm) in surface temperature retrieval has been shown to be useful under certain conditions. For example, Llewellyn-Jones et al. (1984) found that triple window simulations for the tropics were significantly better than split window, but not for temperate latitudes. Barton (1985) found Channel 3 useful in both tropical and midlatitude (Australia) locations. Of course, the use of Channel 3 would be limited to nighttime analyses because it measures reflected solar radiation as well as emitted thermal energy. However, this channel is often noisy at low temperatures when the amount of emitted energy is small, typical of the polar night. Even if the potentially high noise level were not considered, modifying (2) to include Channel 3 reduces the RMSE in the regression by no more than 0.003K for all satellites, which we do not consider a significant improvement in accuracy.

The dependence of the coefficients on sensor scan angle has been found to be important by other investigators (cf. Barton, 1985; Minnett, 1990). This is also the case for IST retrieval, although incorporating both Channels 4 and 5 in (2) reduces the effect that increased path length at large scan angles has on the surface tempera-

ture estimation when scan angle is not taken into account explicitly. Various forms of predictor equations similar to (2) but without the scan angle term were tested, and resulted in increased RMSE values on the order of 0.1 K over using (2). This indicates that including the scan angle in the algorithm provides a small increase in accuracy.

The seasonal and satellite dependence of the coefficients is significant. KH92 demonstrates that errors between 0.1 K and 0.6 K can result when coefficients for one season, or equivalently the temperature ranges used here, are applied to satellite data from another season. Similarly, using coefficients for one satellite with data from another results in errors between 0.1 K and 1.0 K, depending on the temperature range.

Using SST coefficients developed for the North Atlantic (Llewellyn-Jones et al., 1984) and the Greenland Sea area (Minnett, 1990) to estimate IST would result in an underestimate of up to 0.7 K, largest in winter and at scan angles of 40° and greater. Not surprisingly, the difference is much larger, up to a 5.0 K overestimate, when tropical coefficients (Llewellyn-Jones et al., 1984) are used. This comparison was made using simulated radiances based on the directional emissivities, whereas the emissivity of the sea surface in the aforementioned studies was computed by using the Fresnel equations with the refractive index of water. These errors are similar to those reported by Minnett (1986), where SST was retrieved from North Atlantic data using coefficients from other regions. For snow-free land surface temperature retrievals, using the method of Price (1984) with our simulated polar radiance data set resulted in an RMSE 2 K higher than that obtained using (5).

VALIDATION

Previous validation efforts have placed the accuracy of the ice surface temperature algorithm of KH92 in the range of 1–4 K, depending on the season (Key et al., 1994; Yu et al., 1995). The performance of the algorithms presented here is evaluated using satellite data coincident with surface observations at two Arctic locations: an ice camp and a coastal station. The ice camp was part of the Lead Experiment (LeadEx), sponsored by the Office of Naval Research, located in the Beaufort Sea north of Alaska during March and April of 1992. The surface observations of the skin temperature are derived from the upwelling, broadband longwave radiation with an Eppley pyrgeometer. The upwelling longwave flux is corrected for surface reflection of downwelling atmospheric radiation (measured) assuming an emissivity of 0.99; that is,

$$T_{pyrg} = \left(\frac{L_{up} - (1-\varepsilon)L_{down}}{\sigma\varepsilon} \right)^{0.25}, \tag{6}$$

where L_{up} and L_{down} are the upwelling and downwelling longwave flux, σ is the Stefan–Boltzman constant, and ε
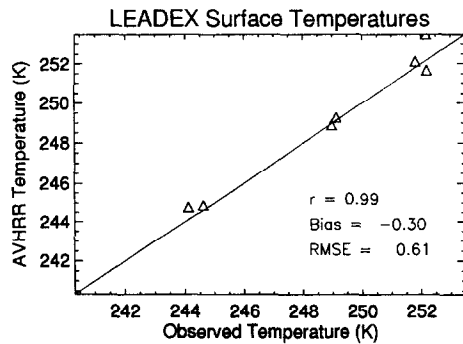
LEADEX Surface Temperatures

Figure 4. Comparison of surface temperatures measured in situ at the LeadEx camp and estimated from the AVHRR. Also given are the linear correlation coefficient, the bias (mean difference between the satellite-derived and surface measurements), and the root-mean-square error.

Validation of Surface Temperature

Figure 5. Comparison of surface temperatures measured in situ at Barrow and estimated from the AVHRR. Also given are the linear correlation coefficient, the bias (mean difference between the satellite-derived and surface measurements), and the root-mean-square error.

is the emissivity. AVHRR-derived and surface-estimated surface temperatures for clear skies during LeadEx are shown in Figure 4.

The temperature retrieval methods were also applied to an annual cycle of AVHRR and ATSR data coincident with surface measurements at Barrow, Alaska. Barrow data were collected by NOAA personnel at the Climate Monitoring and Diagnostic Laboratory (CMDL) baseline observatory. Its coastal location makes comparison with satellite data difficult, especially during the summer when surface ponding is prevalent. It is a very cloudy region and one of high relative humidity. Surface albedo varies from about 0.2 during summer months when snow-free to over 0.8 when snow-covered. The longwave data have been shown to be accurate to within about 1% (Stone et al., 1996). As with the LeadEx data, skin temperatures were computed with (6).

Results are given in Figure 5 for the AVHRR and in Figure 6 for the ATSR. For nonsummer observations, agreement between the surface and satellite-derived temperatures is very good. During the summer, the satellite-derived temperatures are significantly lower. The probable reason for this is the occurrence of ponds, lakes, and coastal waters within the AVHRR or ATSR field of view.

CONCLUSIONS

Methods for the retrieval of the clear sky surface temperature of sea ice, land ice, and snow-free land in the polar regions using AVHRR and ATSR thermal data have been presented. Arctic and Antarctic radiosonde data were used to model sensor radiances. Empirical formulae relating the skin temperature to 11 μm and 12 μm brightness temperatures, emissivities, and the scan angle were then developed. The algorithms presented here are refinements and extensions of that given by KH92 for the sea ice surface temperature.
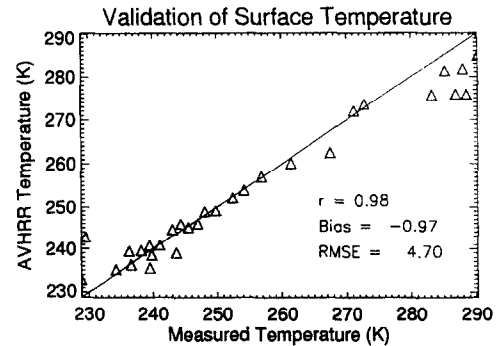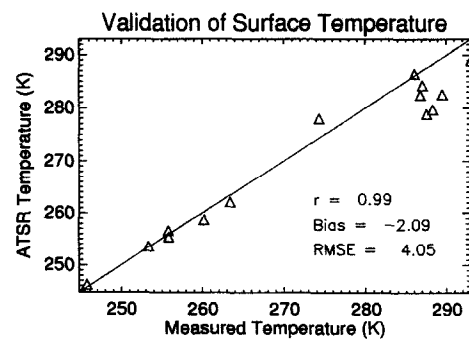
Previous validation efforts have placed the accuracy of the ice surface temperature algorithm of KH92 in the range of 1–4 K, depending on the season. The more extensive validation analysis presented here gives accuracies in the range of 0.3–2.1 K, the larger errors being attributable to the spatially variable surface of the validation area. With the two-direction look, the ATSR algorithms exhibited somewhat smaller RMS errors for both the regression analysis and the validation with surface data, especially at higher temperatures.

Given that the atmospheric correction that forms the basis of the surface temperature estimation is relatively small in the dry polar atmosphere, we believe the primary factor controlling the accuracy of the estimates both here and in KH92 is cloud masking. Even with currently available cloud-masking algorithms, the demonstrated accuracy is sufficient for most climate process studies.

Figure 6. Comparison of surface temperatures measured *in situ* at Barrow and estimated from the ATSR. Also given are the linear correlation coefficient, the bias (mean difference between the satellite-derived and surface measurements), and the root-mean-square error.

Validation of Surface Temperature

REFERENCES

Bamber, J. L., and Harris, A. R. (1994), The atmospheric correction for satellite infrared radiometer data in polar regions. *Geophys. Res. Lett.* 21:2111–2114.

Barton, I. J. (1985), Transmission model and ground-truth investigation of satellite-derived sea surface temperatures. *J. Clim. Appl. Meteorol.* 24:508–516.

Barton, I. J., Zavody, A. M., O'Brien, D. M., Cutten, D. R., Saunders, R. W., and Llewellyn-Jones, D. T. (1989), Theoretical algorithms for satellite-derived sea surface temperatures. *J. Geophys. Res.* 94(D3):3365–3375.

Becker, F., and Li, Z. (1990), Towards a local split window method over land surfaces. *Int. J. Remote Sens.* 11(3):369–393.

Blanchet, J., and List, R. (1983), Estimation of optical properties of arctic haze using a numerical model. *Atmos.-Ocean* 21:444–465.

Connolley, W. M., and King, J. C. (1993), Atmospheric water vapour transport to Antarctica inferred from radiosondes. *Quart. J. Roy. Meteorol. Soc.* 119:325–342.

Dozier, J., and Warren, S. G. (1982), Effect of viewing angle on the infrared brightness temperature of snow. *Water Resourc. Res.* 18(5):1424–1434.

Haefliger, M., Steffen, K., and Fowler, C. (1993), AVHRR surface temperature and narrow-band albedo comparison with ground measurements for the Greenland ice sheet. *Ann. Glaciol.* 17:49–54.

Key, J., and Haefliger, M. (1992), Arctic ice surface temperature retrieval from AVHRR thermal channels. *J. Geophys. Res.* 97(D5):5885–5893.

Key, J., Maslanik, J. A., Papakyriakou, T., Serreze, M. C., and Schweiger, A. J. (1994), On the validation of satellite-derived sea ice surface temperature. *Arctic* 47(3):280–287.

Kneizys, F. X., Shettle, E. P., Abreu, L. W., et al. (1988), Users guide to LOWTRAN 7, AFGL-TR-88-0177, Environmental Research Papers No. 1010, 137 pp.

Lindsay, R. W., and Rothrock, D. A. (1994), Arctic sea ice surface temperature from AVHRR. *J. Clim.* 7(1):174–183.

Llewellyn-Jones, D. T., Minnett, P. J., Saunders R. W., and Zavody, A. M. (1984), Satellite multichannel infrared measurements of sea surface temperature of the northeast Atlantic Ocean using AVHRR/2. *Quart. J. Roy. Meteorol. Soc.* 110:613–631.

McClain, E. P., Pichel, W. G., and Walton, C. C. (1985), Comparative performance of AVHRR-based multichannel on the infrared measurement of sea surface temperatures. *J. Geophys. Res.* 90:11,587–11,601.

Minnett, P. J. (1986), A numerical study of the effects of anom-

alous North Atlantic atmospheric conditions on the infrared measurement of sea surface temperature from space. *J. Geophys. Res.* 91(C7):8509–8521.

Minnett, P. J. (1990), The regional optimization of infrared measurements of sea surface temperature from space. *J. Geophys. Res.* 95(C8):13,497–13,510.

NOAA (1991), *Polar Orbiter Data Users Guide* (K. Kidwell, ed.), U.S. Department of Commerce, National Oceanic and Atmospheric Administration, NESDIS, Washington, DC, 287 pp.

Prata, A. J. (1993), Land surface temperatures derived from the Advanced Very High Resolution Radiometer and the Along-Track Scanning Radiometer 1. Theory. *J. Geophys. Res.* 98(D9): 16,689–16,702.

Prata, A. J. (1994a), Land surface temperatures derived from the Advanced Very High Resolution Radiometer and the Along-Track Scanning Radiometer 2. Experimental results and validation of AVHRR algorithms. *J. Geophys. Res.* 99(D6): 13,025–13,058.

Prata, A. J. (1994b), Land surface temperature determination from satellites. *Adv. Space Res.* 14(3):15–26.

Price, J. C. (1983), Estimating surface temperatures from satellite thermal infrared data—a simple formulation for the atmospheric effect. *Remote Sens. Environ.* 13:353–361.

Price, J. C. (1984), Land surface temperature measurements from the split-window channels of the NOAA 7 Advanced Very High Resolution Radiometer. *J. Geophys. Res.* 89(D5): 7231–7237.

Rees, W. G. (1993), Infrared emissivities of Arctic land cover types. *Int. J. Remote Sens.* 14(5):1013–1017.

Salisbury, J. W., D'Aria, D. M., and Wald, A. (1994), Measurements of thermal infrared spectral reflectance of frost, snow, and ice. *J. Geophys. Res.* 99:24,235–24,240.

Schluessel, P., and Grassl, H. (1990), SST in polynias: a case study. *Int. J. Remote Sens.* 11(6):933–945.

Serreze. M. C., Kahl, J. D., and Schnell, R. C. (1992), Low-level temperature inversions of the Eurasian Arctic and comparisons with Soviet drifting station data. *J. Clim.* 5(6): 615–629.

Sobrino, J. A., Li, Z., Stoll, M. P., and Becker, F. (1994), Improvements in the split-window technique for land surface temperature determination. *IEEE Trans. Geosci. Remote Sens.* 32(2):243–253.

Stone, R., Mefford, T., Dutton, E., Longenecker, D., Halter, B., and Endres, D. (1996), Barrow, Alaska, surface radiation and meteorological measurements: January 1992 to December 1994, NOAA Data Report ERL CMDL-11, Climate Monitoring and Diagnostics Laboratory, Boulder, CO.

Stroeve, J., Haefliger, M., and Steffen, K. (1996), Surface temperature from ERS-1 ATSR infrared thermal satellite data in polar regions. *J. Appl. Meteorol.* 35(8):1231–1239.

Yu, Y., Rothrock, D. A., and Lindsay, R. W. (1995), Accuracy of sea ice temperature derived from the advanced very high resolution radiometer. *J. Geophys. Res.* 100:4525–4532.

Wald, A. (1994), Modeling thermal infrared (2–14 μm) reflectance spectra of frost and snow. *J. Geophys. Res.* 99:24,241–24,250.

Wan, Z., and Dozier, J. (1989), Land-surface temperature measurement from space: physical principles and inverse modeling. *IEEE Trans. Geosci. Remote Sens.* 27(3):268–277.